Acta Astronautica 210 (2023) 535–546

Contents lists available at ScienceDirect

Acta Astronautica

journal homepage: www.elsevier.com/locate/actaastro

Design of an optical system for a Multi-CubeSats debris surveillance mission

Dan Pineau, Leonard Felicetti *

School of Aerospace, Transport and Manufacturing, Cranfield University, UK

ARTICLE INFO

Keywords:
Space debris
Optical system
CubeSats
Design requirements
Constellation

ABSTRACT

The detection and observation of space debris in Low Earth Orbit is generally carried out through the use of ground based radars and telescopes. These instruments allow for a precise reconstruction of the space debris trajectories, and therefore represent a key asset for planning avoidance maneuvers when threats of collisions are predicted.

The recent deployment of mega-constellations, with the consequent increase of the number of satellites, imposes new challenges in terms of simultaneous tracking capability and readiness of the current space situational awareness systems. This adds to the current need to track small and dull objects to further mitigate the probability of triggering cascade collisions. However, ground based observations are limited due to their intrinsic sensibility to atmospheric refraction, their diurnal inoperability and their dependence on meteorological hazards.

This paper proposes to study the feasibility and the benefits of a potential deployment of a constellation of CubeSats in Low Earth Orbit, to acquire optical observations of space debris with enhanced accuracy, as part of the ORCA mission: Orbit Refinement for Collision Avoidance. Here, the focus is on the optical design of the payload instrument to be integrated onboard of the orbiting platforms.

The study trades-off the current state-of-art of optical detection technologies, by assessing their performance against a set of specific requirements: (a) the minimization of the uncertainty associated to the image resolution; (b) a field of view that maximizes the extent of the monitored area; (c) an optimal exposure time to avoid under or overexposure of the image; (d) minimization of the effects of light diffraction and above all, (e) the maximization of the signal to noise ratio to detect the smallest and dullest objects possible.

Several configurations of optical systems are then chosen as suitable for the ORCA constellation, also considering the system design implications of its integration into a CubeSat, such as size requirements. Commercial Off-The-Shelf hardware are explored and performances of the optical system are evaluated through numerical simulations in order to estimate the detectable sizes of space debris while taking into account their potential distances from the sensor. This paper concludes with estimates of the impact of the ORCA mission on space situational awareness for decades to come.

1. Introduction

Run by the US Space Command for the North American Aerospace Defense Command (NORAD), the Space Defense Operation Center (SpaDOC) department of North American Aerospace Defense (NORAD) has been updating a catalogue of space objects ever since to prevent many different sorts of threats under control, such as the atmospheric re-entry of objects or collisions with operational satellites.

As mentioned in [1], the only solution to this problem is the deployment of systems able to automatically detect these objects, identify them and calculate their trajectory so that their positions can be predicted at all times.

The Space Surveillance Network (SSN) has been created for this reason, deployed over 16 sites spread over the world and using different surveillance systems: electronic scanning radars, Ground-based Electro-Optical Deep Space Surveillance systems (GEODSS), and others [2].

However, objects catalogued by SSN are mainly bigger than around 10 cm in LEO, as current techniques hardly allow the tracking of smaller debris. Collisions with debris of this size are severely harmful for any operational satellite. Fortunately, ESA estimates that these debris are too rare to cause a real threat, as a 100 m^2 object in the densest regions of LEO would be hit by 10 cm debris every 1775 years [3]. Nonetheless, ESA's statistical models speculate the presence of around 900,000 debris larger than 1 cm, and 130,000,000 larger than 1 mm [4]. Estimations give one collision per year between debris larger than 1 mm and a 100 m^2 object in the densest regions

* Corresponding author.
E-mail addresses: dan.pineau@universite-paris-saclay.fr (D. Pineau), leonard.felicetti@cranfield.ac.uk (L. Felicetti).

https://doi.org/10.1016/j.actaastro.2023.04.027
Received 9 December 2022; Received in revised form 28 January 2023; Accepted 14 April 2023
Available online 21 April 2023

of LEO. Collisions with these relatively small debris could result in minor damage or neutralization of active satellites depending on impact localization, occurring several times during the average lifespan of most satellites at specific ranges of altitude in LEO.

Smaller and smaller debris can be detected with ever increasing certainty as new projects are launched. For example, projects such as the European Space Surveillance System (ESSS) have been proposed by ESA to exploit current European telescopes and radars, as well as conceiving more efficient instruments, for Europe to create its own space objects catalogue [5]. Current instruments can already detect debris smaller than 10 cm, such as TIRA able to detect 2 cm debris at 1000 km altitude [6], or EISCAT detecting 2 cm objects at 1500 km altitude [7].

However, other kinds of limitations weigh on ground-based observations: diurnal inoperability for optical observations, atmospheric signatures [8], and their dependence on meteorological hazards.

Thus, projects have been launched over the last decade to deploy space-based sensors to (1) detect smaller debris and (2) avoid environmental ground limitations. One of them was Canada's Near-Earth Object Surveillance Satellite (NEOSSat) [9], jointly funded by the Canadian Space Agency (CSA) and the Defense Research and Development Canada (DRDC). It was a low-cost satellite for space surveillance purposes in High Earth Orbit and the world's first satellite to provide surveillance of Near Earth Objects (NEO) as a dual mode. Placed at an altitude of 780 km on a sun-synchronous orbit, it provided useful tracking data to the Space Surveillance Network. When it comes to space surveillance in Low Earth Orbit (LEO), the Space-Based Space Surveillance (SBSS) demonstration mission [10] for Space Surveillance and Tracking (SST) can be mentioned. They successfully demonstrated that micro-satellites could be used to detect and catalogue LEO debris of sizes down to 1 mm, and GEO debris to sizes of 40 cm. The Space-Based Telescopes for Actionable Refinement of Ephemeris (STARE) mission can also be mentioned as part of projects aiming to solve the space debris issue. The project proposed using a constellation of around 12 CubeSats in LEO to spot debris larger than 10 cm before proceeding to the refinement of these debris' orbital parameters [11]. In an attempt to maintain coverage on a wider region of space, launches of space surveillance constellations of CubeSats are expected in the coming years. For example, Northstar [12] plans to launch 52 CubeSats in 2023, whose 12 imaging satellites would be used for space surveillance purposes in LEO [13].

A similar goal is shared with the Orbit Refinement for Collision Avoidance (ORCA) mission [14]. ORCA mission aims at using a network of space-based optical sensors orbiting in a heliosynchronous orbit, as shown in Fig. 1. The overall mission concept was initially proposed in [15] and further expanded to analyze specific aspects of the mission, such as resident space object detection and tracking [16], attitude coordination among spacecraft [17] and algorithms for sharing multiple observations and estimation of the trajectory followed by the observed objects. The concept was further elaborated and expanded in [14], where the business case, the mission analysis, and the design of the CubeSats were proposed and described in detail. However, a detailed design of the payload was missing. The aim of this paper is to demonstrate the feasibility of such an optical system allowing for the detection of resident space objects.

For the frame of this paper, the altitude of ORCA CubeSats is assumed to be 350 km. Such an altitude for the constellation would allow for the coverage of the 350 to 850 km altitude region, within which the density of active payloads is currently the highest in LEO according to ESA's latest annual space environment report [18]. The higher probability of collisions in this region make it of interest as part of the ORCA mission. It is thus necessary for ORCA CubeSats to perform detections at distances up to 500 km. This paper hereby proposes a methodology for selecting and sizing optical systems against a set of requirements imposed by this mission.

The payload top level performance requirements are defined as follows:

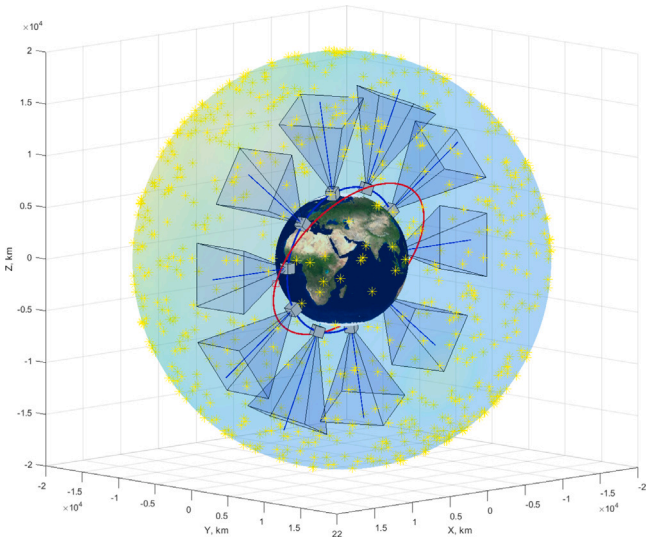

Fig. 1. ORCA constellation concept.

- the payload shall allow the detection of space objects from a distance up to 200 km for objects of sizes down to 5 mm. For distances from 200 km to 500 km, it shall allow the detection of objects down to 1 cm in size.
- the field of view covered by the payload shall be greater than (5°, 5°).

These requirements formulate the need for the detection of objects up to 500 km while guarantying a minimum detection rate using a wide field of view.

The proposed procedure allows for providing a diversity of possible payloads meeting the aforementioned requirements and simultaneously supplies insights into the performance that the optical system will have in orbit. The paper explicitly provides the formulation of useful parameters used to define the key requirements of the ORCA mission, such as the SNR of objects' streaks, as well as their lengths, and their relation with the optical parameters of the payload.

Combinations of Commercial-Off-The-Shelf (COTS) sensor and lenses matching the mission requirements with optimal performances are listed and their potential fit inside CubeSats of a given size is explored.

The remaining parts of the paper are organized as follows: derived technical requirements are described and explained in Section 2. Section 3 describes the pursued methodology to obtain the optimal payload configuration. Finally, Section 4 presents the different results and concludes the payload design to be implemented onboard CubeSats.

2. Optical system model design

This section presents the assumptions and requirements considered for the design of the optical system. It is considered that the attitude of the spacecraft will be determined by a star tracker system, mounted in parallel to the main optical system and sharing the same line of sight. This system will allow the CubeSats to continuously track the same stars over an undefined period of time, thus allowing the stars to appear as clearly defined points on the image. The exposure time chosen for the acquisition of the images will be long enough so that debris will appear as streaks on the image. It is assumed that a straight and bright streak will be the sole condition to accurately detect a debris and estimate its orbit.

The model embeds a set of mission and system requirements that constrain the ranges of values of the optical system design parameters. A total of five categories of requirements are proposed and discussed in the following subsections. The selected parameters of the optical system

should comply with these categories in order to meet the mission objectives, and, at the same time, to assure the feasibility of the system. These are:

- R1: the field of view of the camera, which shall be wide enough to allow an adequate object detection rate;
- R2: the focal ratio of the camera, which shall not be too small to ease the manufacturing process;
- R3: the exposure time, which shall allow streaks to have adequate dimensions for the data to be retrievable;
- R4: the resolution of the camera, which shall allow acceptable accuracy of the measurements;
- R5: the brightness perceived from the object, which shall stay above a specific threshold for it to be detectable.

It is worth noting that, at this stage, the above requirements intentionally do not specify specific thresholds or performance indexes. These values will be provided and justified in Section 3.

The following subsections propose mathematical formulations of these requirements.

2.1. R1: field of view

In opposition to typical space telescopes used for space observation [19], ORCA space debris surveillance CubeSats needs a very wide field of view for the following reasons:

- the larger the space zone covered is, the more space debris are likely to be seen, and therefore fewer CubeSats need to be put into orbit.
- to allow the streaks of the observed objects to fit entirely in the images acquired (see R3 for further details).

In this study, a pinhole camera model is used as a first order approximation to represent the mapping from a 3D to a 2D scene by the camera [20,21].

The aperture angles Φ_1 and Φ_2 defining the rectangular field of view of the camera depend on the sensor dimensions, which are denoted as b_1 and b_2 for the width and the height of the sensor, respectively. The same field of view is also dependent on the focal length, denoted as f. These angles read as [22]:

$$\Phi_1 = 2\arctan\frac{b_1}{2f} \tag{1}$$

$$\Phi_2 = 2\arctan\frac{b_2}{2f} \tag{2}$$

Knowing the minimum fields of view $\Phi_{1,min}$ and $\Phi_{2,min}$ to be covered by the optical system, it is then possible to set two requirements:

$$\Phi_1 > \Phi_{1,min} \tag{3}$$

$$\Phi_2 > \Phi_{2,min} \tag{4}$$

2.2. R2: focal ratio

The focal ratio F, also called F number, is calculated as:

$$F = \frac{f}{D} \tag{5}$$

where D the aperture diameter of the optical system. It can be thought of as the diameter of the effective aperture of the lens of the camera or the diameter of the primary telescope mirror, depending on the chosen instrument [22].

A low value of focal ratio is desirable when the need is to have a large field of view or a greater aperture to increase the image brightness. However, this comes with some drawbacks. Indeed, the lower the F number is, the more the optical system needs to bend the light to make it converge to the sensor, leading to distortions and aberrations. Optical systems that correct such issues are usually extremely expensive.

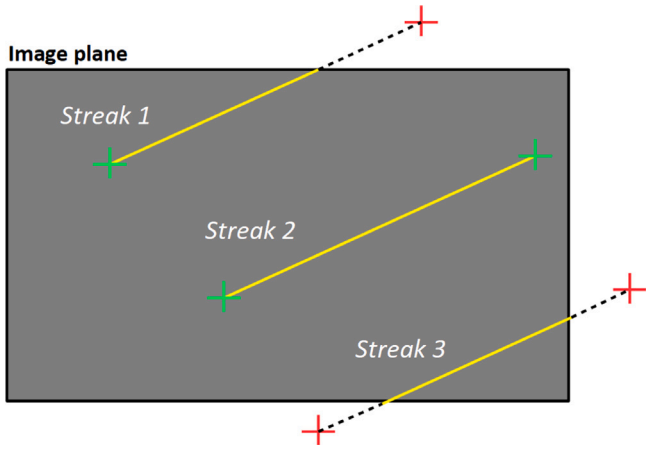

Fig. 2. Three possible cases when acquiring images.

Therefore, the F number of commercially available lenses [23] is usually never found below 0.95. It can also be found that F never exceeds 45.

Thus, it is expected that the focal ratio F of the optical system respects the following inequality:

$$F_{min} < F < F_{max} \tag{6}$$

where $F_{min} = 0.95$ and $F_{max} = 45$.

2.3. R3: length of digital streaks

As explained in the introduction of this section, it is assumed that only streak-like objects will be searched in the image to confirm the detection of an object crossing the field of view of the camera. Indeed, as the ORCA satellite operates image acquisitions in a sidereal tracking, only close and fast-moving objects in the satellite reference frame will appear as streaks. Thus, this detection strategy requires only one image. This feature makes this strategy desirable in terms of computational cost and memory requirements against other methods, such as the stacking method [24]. The downside of the chosen strategy is that debris appearing as dots on the image will be confused with stars. For example, such a case may happen when detected objects are either moving towards the camera or too far away. A lower bound is therefore necessary for the length of streaks in images. On the other hand, too long streaks might not fit entirely in the image, inducing data loss, as illustrated in Fig. 2. Indeed, if one or two streak extremities do not appear in the image plane, as illustrated with Streak 1 and Streak 3 respectively, the full size of the streak cannot be measured. Without the latter information, the space object's orbit cannot be estimated. In this case, orbit determination is only feasible using the data from Streak 2.

The length of a streak L_{st}, as a number of consecutive pixels lining up in the image, must therefore always be contained in an interval $[L_{st,min}, L_{st,max}]$ to increase the chances that it entirely fits within the image. These upper and lower bounds for the streak lengths are given in the following sections.

2.3.1. Upper bound for the streak length

A streak is exploitable when it is entirely contained in the image, as its starting and ending points are necessary for orbit determination purposes.

Knowing the characteristics of the optical system and the objects' parameters at a given instant, it is possible to calculate the probability that the streak created in the resulting image will be fully seen. It is

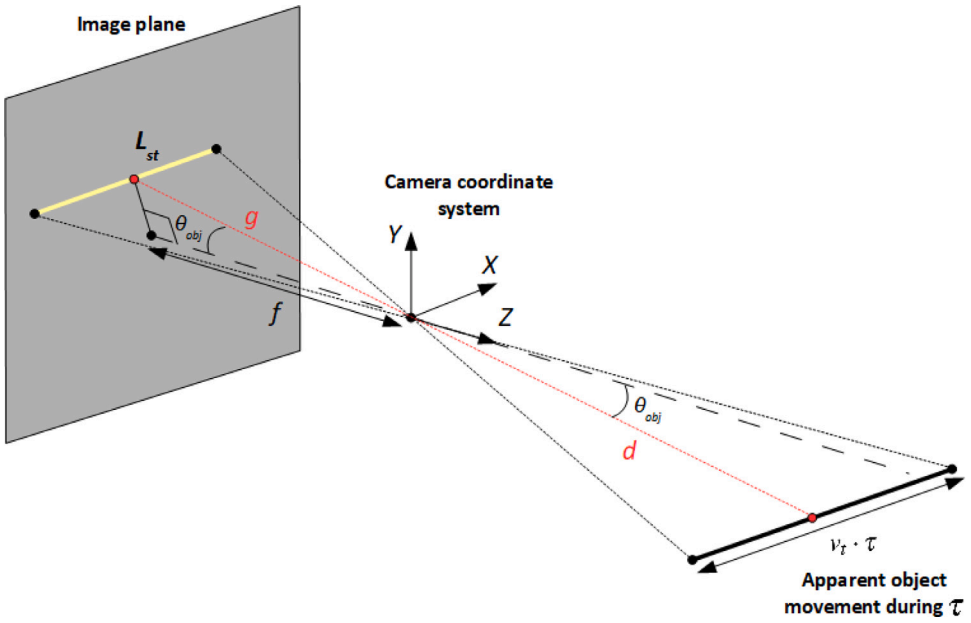

Fig. 3. Formation of a streak on the image plane.

considered that the system respects this requirement if the streak has more than ζ[1] chances to be fully contained in the image.

The onboard camera is pointing and capturing the motion of the object, located at a distance d from the CubeSat. The velocities of the CubeSat and the object are $\vec{v}_{sat}$ and $\vec{v}_{obj}$, respectively. Thus, the relative velocity of the object with respect to the camera is calculated as $\vec{v} = \vec{v}_{obj} - \vec{v}_{sat}$. The relative velocity of the object with respect to the camera can be decomposed as a tangential and a radial component with respect to a reference frame centered in the camera system: $\vec{v} = \vec{v}_t + \vec{v}_r$.

Fig. 3 illustrates how a streak is produced on an image, assuming that the object follows a straight line in the camera coordinate system. The following formulation for the length of a streak L_{st} can be deduced due to the geometry of the situation:

$$L_{st} = \frac{g \cdot v_{t,a} \cdot \tau}{d \cdot p} \tag{7}$$

where τ is the exposure time of the taken image, $v_{t,a}$ is the averaged value of the object tangential velocity v_t in the CubeSat reference frame over τ, p the size of each pixel of the sensor, and d the smallest distance possible between the object and the spacecraft during the acquisition. The term g can be calculated as $g = \frac{f}{\cos(\theta_{obj})}$, and θ_{obj} is the angle between the camera's line of sight and the object's direction as seen from the center of the camera coordinate system.

Therefore, the length of a streak L_{st} can be formulated as:

$$L_{st} = \frac{f \cdot v_{t,a} \cdot \tau}{\cos(\theta_{obj}) \cdot d \cdot p} \tag{8}$$

In a given situation where L_{st} is known, it is possible to calculate the probability P_{in} that this streak will be fully contained in an image of size $h \times w$, where h and w represent the height and width of the image as numbers of pixels, respectively. The probability P_{in} is calculated by the procedure described below.

The following hypotheses are considered for the streaks:

- streaks are straight, and can therefore be represented by a set of two points in $\mathbb{R}^2$: the starting point of the streak X and its ending point Y. X and Y are separated from the distance L_{st}.
- X is always assumed to be already located in the image: X = $(i, j) \in I$, where I is an area defined in $\mathbb{R}^2$ with width w and height h. In other terms, it is assumed that objects are already transiting in the field of view of the system at the beginning of the image acquisition;
- X can be located anywhere in the image with equal probability;
- the orientation of the streaks in the image plane can be in any direction with equal probability.

Considering that a pixel located at the ith row and the jth column is X, I can be mapped by a matrix M_I of size $h \times w$ where each coefficient p_{ij} is the probability that Y is also located in I: $p_{ij} = P(\{X = (i, j)\ ,\ Y \in I\})$. An integration of p_{ij} on the total image area gives the following formulation for P_{in}:

$$P_{in} = \frac{1}{h \cdot w} \sum_{i=1}^{h} \sum_{j=1}^{w} p_{ij} \tag{9}$$

Fig. 4 highlights the distinction of two separate zones in I: an area where any starting point X will lead to a streak of length L_{st} being fully contained in I, called the "safe zone", and an area where this event is uncertain, called the "unsafe zone". These zones are fixed for a given value of L_{st}.

Any pixel in I located at the ith row and the jth column can be thought of as the X extremity of a streak of length L_{st}. The Y extremity of the same streak is therefore located on a circle of center X and radius L_{st}. The location of the circle associated to each pixel (i, j) leads to a specific procedure to calculate p_{ij}. Three different situations are distinguished:

- the circle is fully contained in I, illustrated by circle 1 on Fig. 4;
- one portion of the circle is out of I, illustrated by circle 2;
- two portions of the circle are out of I, illustrated by circle 3;

In the first case, the circle is entirely contained in I because X belongs to the safe zone. For any point located in this region, $p_{ij} = 1$.

The second case happens when X belongs to the unsafe zone. In that case, p_{ij} can be calculated as:

$$p_{ij} = \frac{\omega_{in,ij}}{2\pi} \tag{10}$$

where $\omega_{in,ij}$ is the angle associated to the portion of the circle located inside I. Knowing Δ_{ij}, the distance between the considered pixel and

[1] The variable ζ is a percentage.

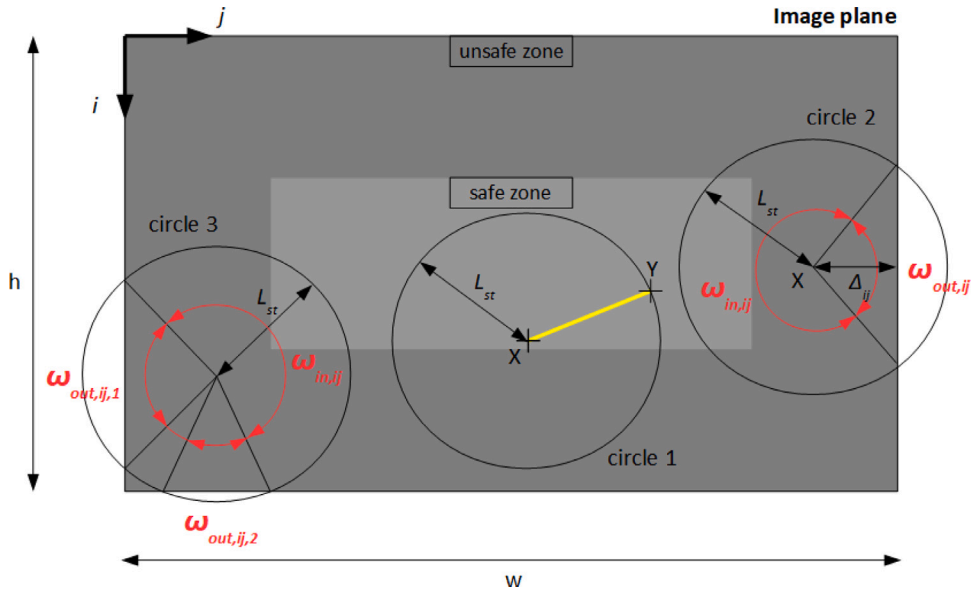

Fig. 4. Representation of the different zones of the image plane and the three different circles of interest.

the border of the image, it is possible to calculate $\omega_{out,ij}$, defined as $\omega_{out,ij} = 2\pi - \omega_{in,ij}$:

$$\omega_{out,ij} = 2\arccos\frac{\Delta_{ij}}{L_{st}} \tag{11}$$

The formulation of p_{ij} for the second case becomes:

$$p_{ij} = 1 - \frac{1}{\pi}\arccos\frac{\Delta_{ij}}{L_{st}} \tag{12}$$

The third case happens when the considered pixel is located in a corner of the unsafe zone. Several portions of the circle are out of I. In that case, two different angles for the portions out of I, $\omega_{out,ij,1}$ and $\omega_{out,ij,2}$, are calculated as previously. Then:

$$\omega_{in,ij} = 2\pi - \omega_{out,ij,1} - \omega_{out,ij,2} \tag{13}$$

and p_{ij} is calculated from Eq. (10).

Other cases where three or four portions of the circle would protrude correspond to streaks longer than the ones studied here. However, the following results demonstrate that streaks of such lengths would have very low probabilities of fitting entirely in I. For this reason, these cases were not explained in this study.

Once p_{ij} has been calculated for every pixel in I, P_{in} is found using Eq. (9). This procedure is useful to know, in a given situation, whether a streak will have a probability P_{in} superior to ζ.

Fig. 5, obtained by repeating the described procedure for many different streak lengths and a fixed image size, demonstrates the evolution of P_{in} with respect to L_{st}. The maximum streak length, $L_{st,max}$, represents the length under which $P_{in} > \zeta = 95\%$, and is easily derived from such a graph. It is important to note that $L_{st,max}$ is fixed for a given image format, i.e. for a given sensor.

Thus, the requirement can be formulated as such:

$$L_{st} < L_{st,max} \tag{14}$$

2.3.2. Lower bound for the streak length

Setting a requirement to impede the streaks from being too small reduces the probability of confusing them with stars, duos of stars, cosmic rays or noise. Such dot-like streaks would be neglected during the image processing procedure, and no data could be retrieved from the corresponding space object.

There is thereby a need to implement a second requirement to the length of streaks by constraining them to be superior to $L_{st,min}$:

$$L_{st} > L_{st,min} \tag{15}$$

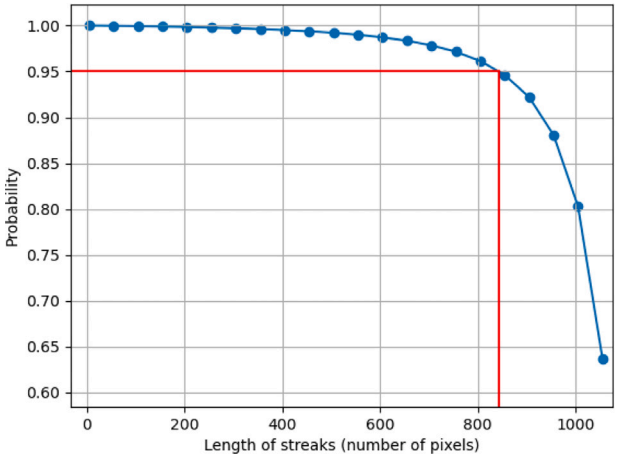

Fig. 5. Probability of streaks entirely contained in the image as a function of their lengths (image size: 2560 × 2160 pixels).

where $L_{st,min}$ is the minimum length of streak that is possible to accept, whose value mainly depends on the subsequently used streak detection algorithms.

2.4. R4: resolution

The images produced by the optical system shall allow to precisely determine the object's position in the image for orbit determination purposes.

Meeting this objective partly depends on the imaging system resolution, which is directly proportional to the number of pixels the sensor is made of and inversely proportional to the size of these pixels [22].

Let us call angular pixel coverage the angle covered by one pixel in the image. Pixels are squares, so this angle is the same for both the angle covered along the height and the width of each pixel.

The wider the angular pixel coverage is, the greater the position uncertainty Δ_p of the observed object is, thus causing high uncertainties in the determined object orbit. As shown in Fig. 6, the maximum position error Δ_p is given by the diagonal of the projection of a pixel on the orthogonal plane at a distance d. The length of such a square δ_p

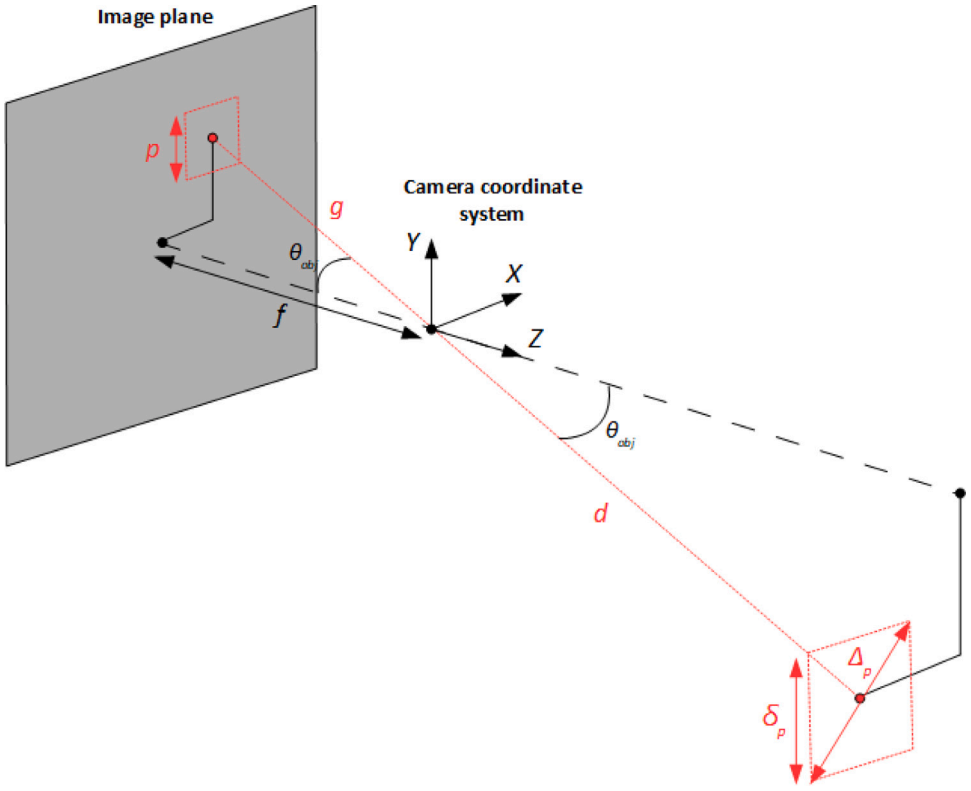

Fig. 6. Representation of the position uncertainty of a point in space.

is:

$$\delta_p = \frac{d \cdot p}{g} = \frac{d \cdot p \cdot \cos(\theta_{obj})}{f} \tag{16}$$

Knowing that $\Delta_p = \sqrt{2}\delta_p$:

$$\Delta_p = \frac{d \cdot p \cdot \cos(\theta_{obj}) \cdot \sqrt{2}}{f} \tag{17}$$

The requirement on the uncertainty Δ_p can be then defined as:

$$\Delta_p < \Delta_{p,max} \tag{18}$$

where $\Delta_{p,max}$ is the upper bound of the allowed position uncertainty for having an accurate estimated orbit.

2.5. R5: signal received

Space debris have various sizes and orientations that generally evolve with time. This results in an unpredictable perceived brightness by the camera. The smaller or the farther the debris is from the camera, the weaker the perceived signal is, and therefore the harder it is to detect the object. A first requirement, defined in Section 2.5.3, can be set to keep the signal received above a threshold, called the detectability threshold, to take into account the sensor limitations.

However, the signal received should not exceed the saturation limit of the sensor. Thus, a second requirement, defined in Section 2.5.4, also sets an upper bound for the signal intensity.

Beforehand, a formulation for the signal received is given in Section 2.5.1.

2.5.1. Calculation of the signal received

Here, the debris is assumed to be a squared plate with side lengths r. Its orientation with respect to the Sun is represented by θ_s, the angle between the normal vector of the plate $\vec{n}$ and a vector $\vec{s}$ sharing the same origin and directed towards the Sun.

According to Lambert's cosine law [25], the solar power received by the object P_r is:

$$P_r = H \cdot r^2 \cdot \cos\theta_s \tag{19}$$

where H is the solar constant ($H = 1361$ W m^{-2}) [26].

The light received by the object is partly reflected in a solid angle $\Omega = 2\pi$ sr (hemisphere). The amount of energy remitted by the object depends on its reflectivity ρ, where ρ is approximated to be constant: $\rho = 0.3$ [27]. The remitted energy by the object per solid angle P_e is deducted as:

$$P_e = \frac{\rho}{2\pi} P_r \tag{20}$$

By denoting θ_c the angle between the normal vector of the plate $\vec{n}$ and a vector $\vec{c}$ sharing the same origin and directed towards the camera aperture center, the power received by the camera is:

$$P_c = P_e \ \cos\theta_c \ \Omega_c \tag{21}$$

where Ω_c is the solid angle directed towards the aperture of the camera from the plate, $\Omega_c = \frac{\pi D^2}{4d^2}$.

Eq. (21) is defined for $(\theta_c, \theta_s) \in [0, 90]^2$ (degrees), while if $\theta_c \leqslant 0$ or $\theta_s \leqslant 0$, then $P_c = 0$. Consequently, P_c can be defined as:

$$P_c = \frac{\rho \cdot H \cdot r^2 \cdot \gamma \cdot D^2}{8d^2} \tag{22}$$

where:

$$\gamma = \begin{cases} \cos\theta_c \cdot \cos\theta_s & \text{if } (\theta_c, \theta_s) \in [0, 90]^2 \text{ (in degrees)} \\ 0 & \text{otherwise.} \end{cases}$$

The average value for γ considering θ_c and θ_s follow uniform distribution over $[0, 90]$ is $\gamma_m = 0.4$. In this study, it is assumed that $\gamma = \gamma_m$.

The total energy received by the camera during the exposure time τ is:

$$E_c = P_c \cdot \tau \tag{23}$$

E_c can be calculated as a number of photons:

$$n_{ph} = \frac{E_c}{h\nu} \tag{24}$$

where $h\nu$ is the energy of a photon where h is the Planck constant ($h = 6.626 \cdot 10^{-34}$ J s) and ν is the wave frequency ($\nu = 600$ THz).

Knowing Q, the quantum efficiency of the sensor, the total number of electrons generated by the sensor as a response to the signal received by the object is:

$$S = Q \cdot n_{ph} \tag{25}$$

Using Eqs. (22)–(24), the expression of S in Eq. (25) becomes:

$$S = \frac{H}{8 \cdot h \cdot \nu} \cdot (\rho \cdot r^2 \cdot \gamma) \cdot \frac{D^2 \cdot \tau}{d^2} \cdot Q \tag{26}$$

where the first fraction is a composition of constants, the second term a composition of parameters related to the observed object, the third one with parameters related to the optical system design, and the last term related to the digital sensor.

2.5.2. Calculation of the sensor noise

The total number of electrons generated from all the illuminated sensor pixels, N, is assumed to be the sum of independent Gaussian noises [28]. N can therefore be expressed as:

$$N = \sqrt{\sigma_{sky}^2 + \sigma_{shot}^2 + \sigma_{dark}^2 + \sigma_R^2} \tag{27}$$

where σ_{sky}, σ_{shot}, σ_{dark} and σ_R are the standard deviations of the sky background noise, the shot noise, the dark noise and readout noise measured by the sensor in the illuminated zone during the exposure time τ, respectively.

By denoting n_{ip} the number of illuminated pixels on the sensor, the noise variances can be formulated as follows:

$$\sigma_{shot}^2 = S \tag{28}$$

$$\sigma_{sky}^2 = K \cdot n_{ip} \cdot \tau \tag{29}$$

$$\sigma_{dark}^2 = I_{dark} \cdot n_{ip} \cdot \tau \tag{30}$$

$$\sigma_R^2 = R_N^2 \cdot n_{ip} \tag{31}$$

where $K = 0.01$ e^- s^{-1} pixel^{-1}, the sky count rate per pixel [29]; I_{dark} is the dark current flowing in a given sensor (e^- s^{-1} pixel^{-1}); R_N the readout noise for a given sensor (e^- pixel^{-1}).

This gives an explicit formulation for N:

$$N = \sqrt{S + n_{ip} \cdot ((K + I_{dark}) \cdot \tau + R_N^2)} \tag{32}$$

The number of illuminated pixels on the sensor n_{ip} can be approximated by the product of the length of the streak L_{st} by its width W_{st}:

$$n_{ip} = L_{st} \cdot W_{st} \tag{33}$$

where L_{st} is calculated using Eq. (8) and W_{st} depends on light diffraction through the camera lenses. Indeed, every lens induces the formation of diffraction patterns on the output image, known as Airy pattern [22]. The centered and brightest disk at the center of such a pattern is called the Airy disk, which W_{st} depends on.

The radius of the Airy disk R_{airy} is known to be [22]:

$$R_{airy} = 1.22 \cdot \lambda \cdot F \tag{34}$$

where λ is the wavelength and F is the F number of the optical system.

Therefore, the width of the streak is:

$$W_{st} = \frac{2R_{airy}}{p} \tag{35}$$

and Eq. (33) becomes:

$$n_{ip} = (2.44 \cdot \lambda) \cdot \frac{v_{t,a}}{\cos(\theta_{obj}) \cdot d} \cdot \frac{\tau \cdot f^2}{D} \cdot \frac{1}{p^2} \tag{36}$$

2.5.3. Signal to noise ratio

The greater the signal received is compared to the mean level of noise of the image, the easier it will be for image processing algorithms to detect the object. If the signal received is comparable to the mean level of noise, the object is at risk of being left undetected. The proposed requirement for the system design maintains the probability of detecting a transiting object above a chosen threshold. The ratio of this averaged streak intensity to the mean level of noise measured in the illuminated pixels of the streak gives its averaged signal to noise ratio, called $R_{S/N}$.

From [28], it can be deduced that a formula for the streak averaged signal to noise ratio $R_{S/N}$ is:

$$R_{S/N} = \frac{S}{N} \tag{37}$$

where formulations for S and N were given from Eqs. (26) and (32), respectively.

The necessary requirement for streak detectability is:

$$R_{S/N} \geqslant R_{S/N,min} \tag{38}$$

where $R_{S/N,min}$ is the minimum signal to noise ratio under which algorithms cannot detect the streaks.

2.5.4. Saturation

Each pixel of a digital sensor generates a signal whose intensity is proportional to the number of accumulated photons during the exposure time τ. However, pixels can only store a finite number of photons before their conversion into electrons. If a pixel saturates, "blooming" might occur [30].

Let T be the total number of electrons generated by the sensor in its illuminated area at the end of an observation and C the pixel well depth.

Assuming the streak and noise intensities are homogeneous in the illuminated area of the sensor, the requirement to avoid the saturation of a pixel is:

$$T < n_{ip} \cdot C \tag{39}$$

where $T = S + N$.

In reality, the streak and noise intensities are not homogeneous as the central pixels are usually brighter than the peripheral ones. However, the saturation of only a few pixels of the streak during observations would not have significant consequences. It has been chosen that the saturation problem would not have significant consequences for the image quality if:

$$T < \chi \cdot n_{ip} \cdot C \tag{40}$$

where χ is the saturation threshold.

3. Optical system selection strategy

This section describes the chosen methodology to find the optimal optical system for the mission.

To observe a specific object of size r and tangential velocity v_t at a distance d, an optical system with focal length f and aperture diameter D, working with an exposure time τ, is considered a feasible solution if and only if the system complies with all the requirements described in Section 2.

In this study, a digital sensor whose parameters are given in Table 1 was chosen. The following values for the different thresholds used in the predefined requirements, R1 to R5, were chosen as follows:

- R1: the values of the angles of the field of view along the two dimensions are $\Phi_{1,min} = 5°$, and $\Phi_{2,min} = \Phi_{1,min} \cdot \frac{b_2}{b_1} \approx 4.96°$ to fit with the sensor's dimensions;
- R2: the boundary values for the focal ratio are $F_{min} = 0.95$ and $F_{max} = 45$, as explained in Section 2.2;

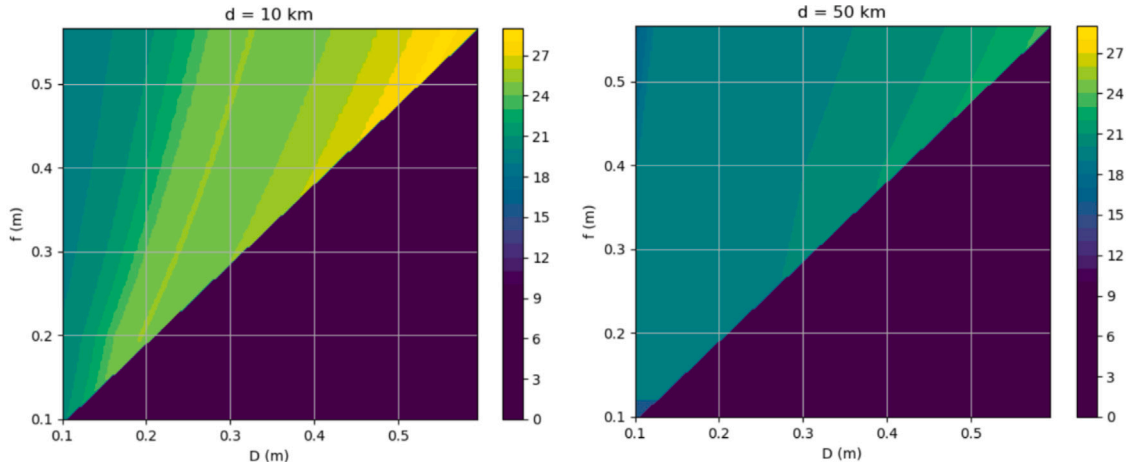

(a)

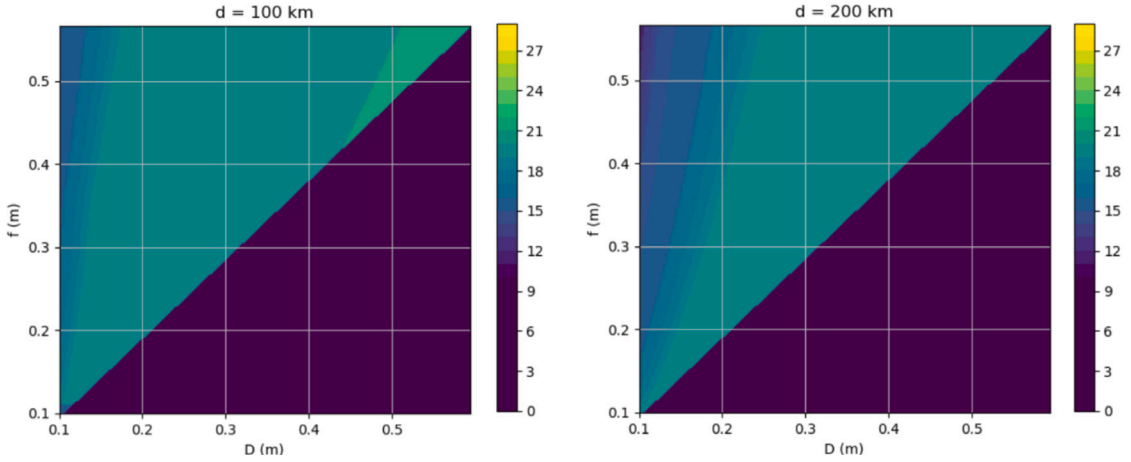

(b)

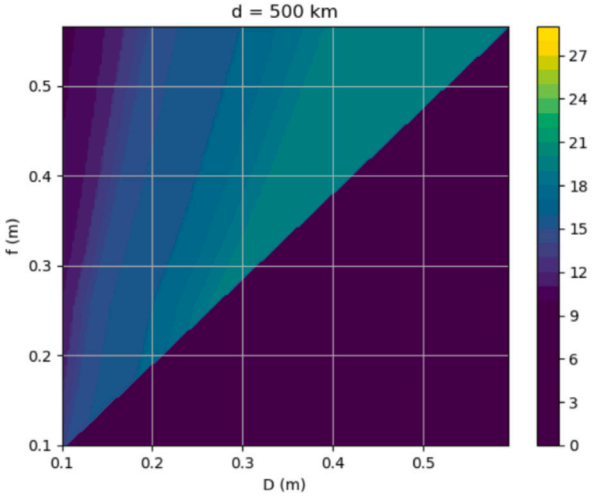

(c)

Fig. 7. Score of each optical system for $d = 10$, 50, 100, 200 and 500 km when using their optimal τ.

- R3: for any streak to have a probability $\zeta = 95\%$ of fitting within the sensor of the Balor (Table 1), it needs to have a maximum length of $L_{st,max} = 1493$ pixels (value found using the procedure explained in Section 2.3.1). The streaks will have a minimum length of $L_{st,min} = 50$ pixels to allow for image processing algorithms to detect them;
- R4: the allowed position uncertainty is $\Delta_{p,max} = 500$ m;
- R5: the minimum signal to noise ratio is $R_{S/N,min} = 5$, and the saturation threshold $\chi = 0.9$.

These requirements allowed to conduct a parametric study to find which optical systems would be able to detect debris in most cases, i.e. which set of optical system parameters would meet all requirements at the same time for most of the scenarios. A scenario is here defined with three parameters: the size of the object r, its relative tangential

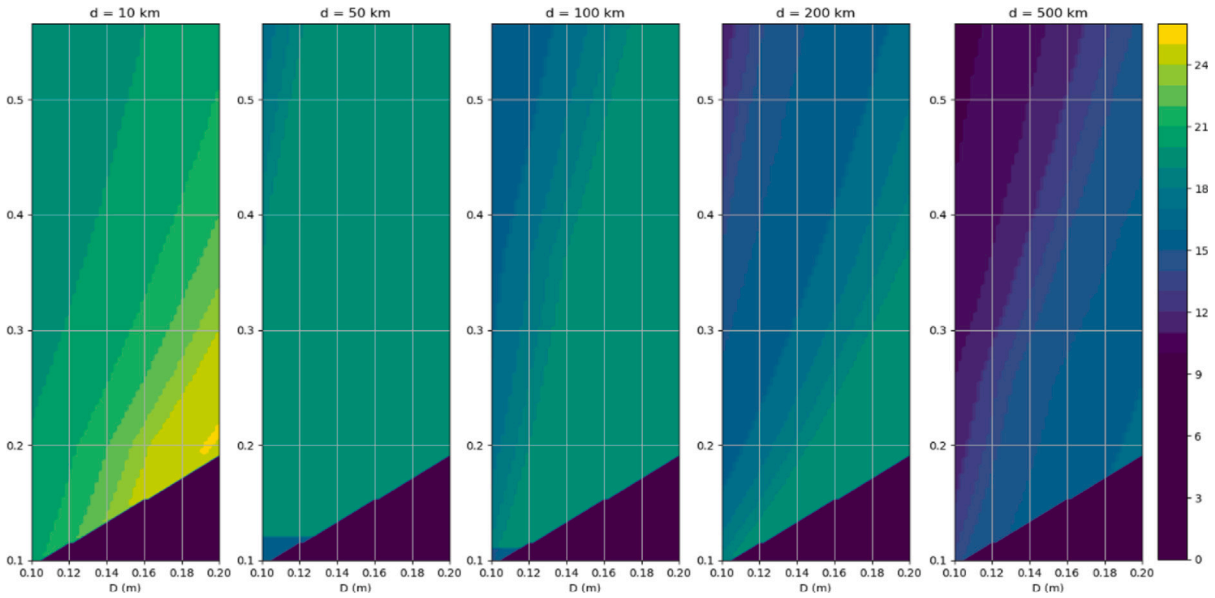

Fig. 8. Score for all optical system with $D < 20$ cm for all distances when using their optimal τ.

Table 1
Balor digital sensor parameters [30].

Parameter	Value
Sensor size $b_1 \times b_2$	49.5 mm × 49.2 mm
Active pixels	4128 × 4096
Pixel size p	12 µm
Peak quantum efficiency Q	61%
Pixel well depth C	80.000 electrons
Readout noise R_N	4.3 electrons
Dark current I_{dark}	0.03 e^- s^{-1} $pixel^{-1}$

Table 2
Scores of five different optical systems.

Optical system parameters			d (km)					Total score
F	f (mm)	D (mm)	10	50	100	200	500	
5	500	100	20	17	16	12	10	75
4	500	125	20	20	17	15	11	83
4	400	100	20	19	16	14	11	80
2.8	400	142.8	21	20	19	16	12	88
2.8	300	107.1	20	20	17	16	12	85

velocity $v_{t,a}$, now noted v, and its distance w.r.t. the CubeSat d. This experiment consisted in:

- assigning a score, equal to 0, for each optical system represented by the 3 parameters f, D, and τ;
- for each scenario, represented by the 3 parameters r, v, and d, adding 1 to the score of the corresponding optical system when all five requirements are met at the same time.

The optical systems with the best scores are therefore considered "optimal" in terms of detection versatility, and their selection is presented in Section 4.

The boundary values for each of the 6 iterated variables, i.e. f, D, τ, r, v, and d, were purposely chosen to represent a wide variety of optical systems and scenarios.

Objects with side lengths r smaller than 0.1 mm were assumed to be undetectable in this context, and objects larger than 10 cm are already detectable from ground-based space surveillance systems. Seven different values were considered between 0.1 mm and 10 cm: 0.1 mm, 0.5 mm, 1 mm, 5 mm, 10 mm, 50 mm, and 100 mm. The range of relative velocities between the objects and the sensors might sensibly vary based on the different relative configurations of the orbits. For this reason, we consider the following relative tangential velocities v of space objects in the sensor's reference frame: 1 km s^{-1}, 3 km s^{-1}, 5 km s^{-1}, 7 km s^{-1} and 9 km s^{-1}. Finally, the following values for the distance d between the sensor and space objects are as follows: 10 km, 50 km, 100 km, 200 km, 500 km. Therefore, 35 (7 × 5) scenarios per distance are considered in this study.

Regarding the optical system parameters, the considered aperture diameter D and the focal length f of the optical system were chosen in the range $[0.1, 0.6]$ m, with a step of 0.002 m, and the exposure times τ in the range $[0.001, 5]$ s, with a step of 0.001 s.

4. Results

In this section, the results of the parametric analysis are presented with the aim of finding the optical systems with the best score for the 35 observation scenarios considered.

Fig. 7 shows the scores for all possible optical systems located at distances $d = 10$, 50, 100, 200, and 500 km from debris. Note that, for this figure and for each couple of parameters f and D, the value of τ was chosen to maximize the associated score. This choice was maintained for the following figures.

It is worth noting that the maximum amount of detectable debris naturally decreases when d increases: 29/35 when $d = 10$ km, 24 for 50 km, 21 for 100 km, and 20 for 200 km and 500 km. Scores increase mainly w.r.t. the aperture diameter D for a fixed focal length f. Such results can intuitively be understood knowing that a higher D allows more light to enter the optical system, ultimately increasing the signal to noise ratio, as in Eq. (37), and therefore the chances of detecting fainter objects.

Moreover, given a fixed aperture diameter D, the number of detectable objects decreases as the focal length f increases. Indeed, greater focal lengths correspond to narrower fields of view leading to decrease the likeliness that streaks can fall entirely into them, as shown in Eq. (14).

Fig. 8 shows the results under the assumption that a specific upper boundary on the aperture diameter $D_{max} = 20$ cm is set in order to fit within a standard CubeSat form factor, e.g. 12U, 16U.[2]

[2] 1U = 10 cm × 10 cm × 10 cm.

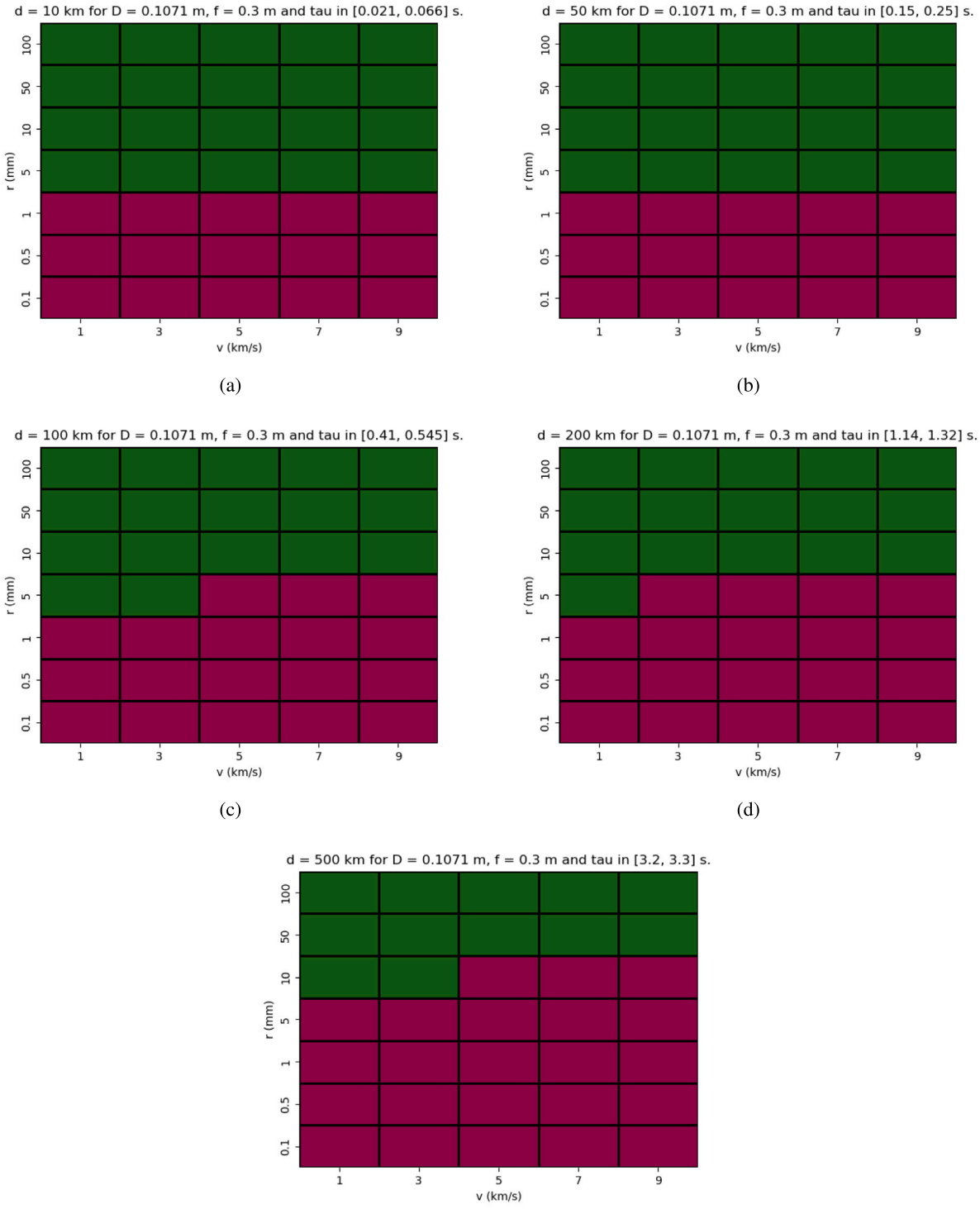

Fig. 9. Debris detected by the second best optical system for each distance. Green rectangle: debris detected; Purple rectangle: debris left undetected. (For interpretation of the references to color in this figure legend, the reader is referred to the web version of this article.)

The maximum score possible decreases when d increases: 26 for 10 km, 20 for 50 km, 100 km, and 200 km, and finally 17 for 500 km. These optimal regions are generally located at the bottom-right hand corner of the five figures, where systems with the smallest focal ratio F and the highest aperture diameter D can be found. In this case, $D = 20$ cm and $f = 19$ cm.

A database of COTS lenses was exploited to find lenses whose characteristics fit within the parameters ranges defined for this study [23].

Five different settings of optical system dimensions were found and reported in Table 2. The same table reports the scores that would be obtained using these settings for each distance, while using them at their optimal τ.

Table 3
COTS lenses matching the optimal configuration for the ORCA mission.

Lens name	Length	Max. aperture	Score (Table 2)	Min. volume of hosting CubeSat
Canon EF 400 mm f/2.8L IS II USM	343 mm	163 mm	88	16U
Nikon AF-S Nikkor 400 mm F2.8G ED VR	368 mm	160 mm		
Nikon AF-S Nikkor 400 mm f/2.8E FL ED VR	358 mm	159.5 mm		
Nikon AF-S Nikkor 300 mm f/2.8G ED VR II	267.5 mm	124 mm	85	12U
Canon EF 300 mm f/2.8L IS II USM	248 mm	128 mm		
Canon EF 300 mm f/2.8L IS USM	252 mm	128 mm		
Sony 300 mm F2.8 G II	242.5 mm	122 mm		

The optical system configuration $F = 2.8$ and $f = 400$ mm has the highest score for each distance, resulting in the highest overall score (88/175). No different debris could be detected using other systems, proving that this system is the best among the one proposed.

These results prove that, using COTS optical technology, it is possible to detect debris of sizes down to 1 mm at close range ($d = 10$ km), 5 mm at medium ranges ($d = 50$, 100 and 200 km) and 1 cm for longer ranges ($d = 500$ km), therefore meeting the performance criteria for the ORCA mission.

For such a configuration, the lengths and maximum diameters range from 343 to 368 mm and from 159.5 to 163 mm as seen in Table 3, respectively. As a result, such kinds of lenses could only be hosted in CubeSats whose dimensions are greater than 34.3 × 16 × 16 cm, i.e. approximately 16U volume.

If a CubeSat of such a size is not suitable for practical and economical reasons, smaller lenses should be considered, such as the ones matching with the second best optical system configuration in Table 2. Lengths and maximum diameters for these lenses range from 242.5 to 267.5 mm and from 122 to 128 mm as seen in Table 3, respectively.

Such an optical system configuration would therefore suit the mission for two reasons:

- the system would fit in a 12U CubeSat, which is known to be a standard format [31];
- the system meets the top level performance requirements defined in the introduction of this chapter. Indeed, as illustrated in Fig. 9, it can be seen that for distances d ranging from 10 to 200 km, objects down to a size of 5 mm could be detected, and at 500 km, objects of 1 cm could be spotted.[3]

5. Conclusion

The needs of the Orbit Refinement for Collision Avoidance (ORCA) mission were formalized as specific and measurable requirements for the design of optical systems onboard CubeSats. The dependency of these requirements on the sizing and acquisition settings of the optical systems allowed to conduct a parametric study to find the combination of optical system parameters that would meet the mission requirements. Among them, a selection was carried out to find the optical systems that could detect debris in the widest range of observation scenarios.

A comparison of these findings with known COTS optical systems validated the feasibility of such systems. Using a digital sensor dedicated for space observations mounted in a 12U CubeSat, it was found that lenses with focal lengths 300 mm and focal ratio f/2.8 would be optimal to detect the greatest range of different debris with sizes from 5 mm to 10 cm, relative velocities from 1 to 9 km/s, and distances from the sensor from 10 to 500 km.

The detection of such debris would favor the successful execution of orbit determination algorithms to predict their trajectories and estimate probabilities of collision. Therefore, collisions in LEO could be prevented in accordance to the ORCA mission, improving our current space situational awareness capabilities for decades to come.

[3] Note that this result are true only for the specific object velocities, as shown Fig. 9.

Declaration of competing interest

The authors declare that they have no known competing financial interests or personal relationships that could have appeared to influence the work reported in this paper.

Acknowledgment

The authors would like to thank Andor Technology for providing essential resources on COTS digital sensors for space observation.

References

[1] celestrak.com, https://celestrak.com/. (Accessed: 24 July 2021).
[2] R. Sridharan, A.F. Pensa, US space surveillance network capabilities, in: Image Intensifiers and Applications; and Characteristics and Consequences of Space Debris and Near-Earth Objects, Vol. 3434, International Society for Optics and Photonics, 1998, pp. 88–100, http://dx.doi.org/10.1117/12.331225.
[3] H. Klinkrad, P. Beltrami, S. Hauptmann, C. Martin, H. Sdunnus, H. Stokes, R. Walker, J. Wilkinson, The ESA space debris mitigation handbook 2002, Adv. Space Res. 34 (5) (2004) 1251–1259, http://dx.doi.org/10.1016/j.asr.2003.01.018.
[4] ESA, ESA'S annual space environment report, GEN-DBLOG-00288-OPS-SD, 2022.
[5] T. Donath, T. Schildknecht, P. Brousse, J. Laycock, T. Michal, P. Ameline, L. Leushacke, Proposal for a European space surveillance system, in: 4th European Conference on Space Debris, Vol. 587, 2005, p. 31.
[6] D. Cerutti-Maori, J. Rosebrock, C. Carloni, M. Budoni, I. Maouloud, J. Klare, A novel high-precision observation mode for the tracking and imaging radar TIRA–principle and performance evaluation, in: 8th European Conference on Space Debris, ESA/ESOC, Darmstadt, Germany, Virtual Conference, 2021.
[7] G. Wannberg, I. Wolf, L.-G. Vanhainen, K. Koskenniemi, J. Röttger, M. Postila, J. Markkanen, R. Jacobsen, A. Stenberg, R. Larsen, et al., The EISCAT svalbard radar: A case study in modern incoherent scatter radar system design, Radio Sci. 32 (6) (1997) 2283–2307, http://dx.doi.org/10.1029/97RS01803.
[8] T.S. McKechnie, Light propagation through the atmosphere and the properties of images formed by large ground-based telescopes, J. Opt. Soc. Amer. A 8 (2) (1991) 346–365.
[9] V. Abbasi, S. Thorsteinson, D. Balam, J. Rowe, D. Laurin, L. Scott, M. Doyon, The neossat experience: 5 years in the life of Canada's space surveillance telescope, in: 1st NEO and Debris Detection Conference, Vol. 22, 2019.
[10] J. Utzmann, A. Wagner, Sbss demonstrator: a space-based telescope for space surveillance and tracking, 2015.
[11] L. Simms, W. Vries, V. Riot, S. Olivier, A. Pertica, B. Bauman, D. Phillion, S. Nikolaev, Space-based telescopes for actionable refinement of ephemeris pathfinder mission, Opt. Eng. 51 (2012) http://dx.doi.org/10.1117/1.OE.51.1.011004, 1004–.
[12] D. O'Connell, D.R. Peddle, S. Bain, D.W. Bancroft, K. Stakkestad, The NorthStar system—a new era in earth observation, in: 2017 IEEE International Geoscience and Remote Sensing Symposium, IGARSS, IEEE, 2017, pp. 451–454, http://dx.doi.org/10.1109/IGARSS.2017.8126991.
[13] Newspace.im, https://www.newspace.im/constellations/northstar. (Accessed: 21 January 2023).
[14] A. Barles, S. Bilkhu, A. Boulnois, F.J.C. Arija, G.D. Albacete, W. Easdown, A.E. Silvela, R.G. Fernández, B. Kent, J.M. Mariscal, et al., Mission ORCA: Orbit refinement for collision avoidance, Adv. Astronaut. Sci. Technol. (2022) 1–17, http://dx.doi.org/10.1007/s42423-022-00106-8.
[15] L. Felicetti, M.R. Emami, A multi-spacecraft formation approach to space debris surveillance, Acta Astronaut. 127 (2016) 491–504, http://dx.doi.org/10.1016/j.actaastro.2016.05.040.
[16] L. Felicetti, M.R. Emami, Vision-aided attitude control for space debris detection, J. Guid. Control Dyn. 41 (2) (2018) 573–575, http://dx.doi.org/10.2514/1.G002884.
[17] L. Felicetti, M.R. Emami, Attitude coordination of multiple spacecraft for space debris surveillance, Adv. Space Res. 59 (5) (2017) 1270–1288, http://dx.doi.org/10.1016/j.asr.2016.12.012.

[18] S. Lemmens, F. Letizia, ESA's annual space environment report, Technical Report GEN-DB-LOG-00288-OPS-SD, ESA Space Debris Office, 2022.
[19] V.Y. Terebizh, Survey Telescope Optics, 2019.
[20] N. Van Oosterwyck, Real time human robot interactions and speed control of a robotic arm for collaborative operations, 2018, http://dx.doi.org/10.13140/RG.2.2.28723.53286.
[21] P. Corke, Robotics, Vision and Control: Fundamental Algorithms in MATLAB, first ed., Springer Publishing Company, Incorporated, ISBN: 3642201431, 2013.
[22] W. Larson, J. Wertz, Space Mission Analysis and Design, Microcosm, 1992.
[23] DXOMARK, https://www.dxomark.com/Lenses/. (Accessed: 12 June 2021).
[24] T. Yanagisawa, H. Kurosaki, A. Nakajima, Jaxa's optical observation facility for space debris observation and its activities, Trans. Japan Soc. Aeronaut. Space Sci. 8 (ists27) (2010) Pr_2_49–Pr_2_53, http://dx.doi.org/10.2322/tastj.8.Pr_2_49.
[25] J. Folkesson, H. Chang, N. Bore, Lambert's cosine law and sidescan sonar modeling, in: 2020 IEEE/OES Autonomous Underwater Vehicles Symposium, AUV, 2020, pp. 1–6, http://dx.doi.org/10.1109/AUV50043.2020.9267946.
[26] G. Kopp, J. Lean, A new, lower value of total solar irradiance: Evidence and climate significance, Geophys. Res. Lett. 38 (2011) http://dx.doi.org/10.1029/2010GL045777.
[27] D. Kessler, K. Jarvis, Obtaining the properly weighted average albedo of orbital debris from optical and radar data, Adv. Space Res. (ISSN: 0273-1177) 34 (5) (2004) 1006–1012, http://dx.doi.org/10.1016/j.asr.2003.02.030, Space Debris.
[28] T. Schildknecht, U. Hugentobler, A. Verdun, Algorithms for ground based optical detection of space debris, Adv. Space Res. (ISSN: 0273-1177) 16 (11) (1995) 47–50, http://dx.doi.org/10.1016/0273-1177(95)98752-A, Space Debris.
[29] Space Telescope Science Institute, Signal-to-noise ratio estimation, 2020, https://www.stsci.edu/instruments/wfpc2/Wfpc2_hand_current/ch6_exposuretime6.html. (Accessed:17 December 2020).
[30] Andor Oxford Instruments, https://andor.oxinst.com/. (Accessed:13 December 2020).
[31] Endurosat, 12U CubeSat platform datasheet, 2021, https://www.endurosat.com/cubesat-store/cubesat-platforms/12u-cubesat-platform/. (Accessed: 15 September 2021).

Design of an optical system for a Multi-CubeSats debris surveillance mission

Pineau, Dan

2023-06-13

Pineau D, Felicetti L. (2023) Design of an optical system for a Multi-CubeSats debris surveillance mission. Acta Astronautica, Volume 210, September 2023, pp. 535-546
https://doi.org/10.1016/j.actaastro.2023.04.027